SIMO Extension of the Algorithm of Mode Isolation

M. S. Allen, and J. H. Ginsberg
The G. W. Woodruff School of Mechanical Engineering
Georgia Institute of Technology
Atlanta, GA 30332-0405

October 10, 2003

Abstract

Many multi-degree-of-freedom (MDOF) modal analysis algorithms make use of a stabilization diagram to locate system modes. The algorithm of mode isolation (AMI) provides an alternative approach in which modes are identified and subtracted from the data one at a time. An iterative procedure then refines the initial estimate. Previous work has shown that AMI gives good results when compared to other MDOF algorithms. This work presents an extension of AMI in which the frequency response functions (FRFs) from all measurement points are considered simultaneously, resulting in global estimates for natural frequencies and damping ratios, and consistent mode vectors. A linear-least-squares, frequency domain, global, SIMO, SDOF fitting algorithm is derived and tested using noise contaminated analytical data. Comparisons with the rational fraction polynomial algorithm (RFP-SIMO) and the stochastic subspace identification algorithm (SSI) show that AMI performs favorably.

1 Nomenclature

$H_{jP}(\omega)$	FRF for displacement j due to excitation P
H_c	Composite FRF
$\{A_{P,r}\}$	Modal residue vector for the rth mode driven at P
λ_r	rth eigenvalue
$\{\phi_r\}$	rth displacement mode vector (Normalized)
ω_r	rth natural frequency
ζ_r	rth modal damping ratio
$\{q\}$	Generalized coordinates
$\{\psi_r\}$	rth state space mode vector (Normalized)
w	Transverse displacement
θ	Torsional rotation
ω	Drive frequency

2 Introduction

Allemang [1] stated: "The estimation of an appropriate model order is the most important problem encountered in modal parameter estimation." Model order determination comprises much of the user interaction involved in experimental modal analysis [2].

The objectives in experimental modal analysis differ from those in general system identification, in that the goal is meaningful modes of vibration, rather than matching of input and output data. Virtually all MDOF identification algorithms return a number of computational modes intermixed with the true system modes. There are two considerations in finding an appropriate model order: Finding the order that gives the most accurate modal parameters for the true system modes, and distinguishing true system modes from computational ones.

Plots of singular values (as in ERA or SSI for example [3],[4],[5]) or error charts [2] [1] may suggest a model order that results in modal parameters that are accurate enough for many purposes, though optimality has not been studied. Careful inspection of a stabilization diagram will give an indication of the magnitude of variance from one model order to the next, but bias errors that are stable relative to model order are more difficult to detect. In this work, stabilization diagrams generated by the Stochastic Subspace Algorithm (SSI) will be examined for an indication of bias and variance errors. It will be shown that the SSI algorithm tends to give a false sense of security regarding the accuracy of the modal parameters. Furthermore, the best accuracy can only be obtained if significant computational resources are available.

The stabilization diagram is also the primary tool for distinguishing computational modes from true system modes. There are a number of tools available to assist in this. Goethals and De Moor [6] found that energy could be used to distinguish many of the spurious modes. Verboven et al [7] used pole characteristics as well as properties of the stabilization diagram, such as the variation in a pole's frequency from one model order to the next, to detect spurious modes. While these represent substantial aides, an absolute criteria for detecting spurious modes for a general problem has not been developed. A common approach is to use a stabilization diagram, combined with mode indicator functions, such as the complex mode indicator function (CMIF), to manually extract true modes from the MDOF algorithm's output. In some frequency ranges, stable modes may not be visible [8]. Furthermore, none of these methods assess the effect of computational modes on the accuracy of true system modes.

The algorithm of mode isolation (AMI) offers a different perspective on the problem of finding the true modes of a system. In AMI, modes are extracted one at a time, and then subtracted from the data. In this process the importance of each mode in the fit is clearly visible. The number of true modes in the data set is then taken to be the number of modes that must be fit to the data to reduce it to noise. An iterative procedure then refines the initial estimate. The resulting MDOF fit does not include any spurious or computational modes. Previous work [9], [10] has shown that AMI gives substantially more accurate results when compared to some other MDOF algorithms that fit a system with a number of model orders and then later try to extract meaningful results. Furthermore, the conditions under which the problem is ill conditioned are revealed.

Because modes are identified one at a time, only a single degree of freedom fit is needed, which makes the algorithm computationally efficient, with small workspace requirements. AMI can be used whenever an FRF can be represented as a sum of poles with associated residues. For example, Joh and Lee [11] suggested a procedure similar to AMI to simplify the identification of rotordynamic systems. Another possible extension might be to aid in finding frequency domain models for viscoelastic systems, as in [12].

The primary new feature of the present work is its implementation of a refined technique for fitting individual modes. Ginsberg *et al* [13] derived a linear-least-squares fitting procedure that is exact for noise-free data. That technique used only a single FRF. The present work extends the previous development to obtain a set of parameters that simultaneously best fit all FRFs.

3 The Algorithm of Mode Isolation

AMI was first presented by Drexel and Ginsberg [9], although it was previously suggested by Joh and Lee [11]. Improvements to the algorithm and the results of test problems are documented in [14], [15], [16], [13] and [17]. AMI is based upon the recognition that the FRF data to be fit is a superposition of individual modal contributions. AMI identifies each mode individually, and then subtracts its contribution from the data. Once all of the modes have been subtracted, only noise remains, thereby identifying the model order as the number of modes subtracted before the data is reduced to noise. An iterative procedure is then used to refine the initial estimate in order to account for overlapping contributions of adjacent modes. The algorithm also provides a self-correcting check that the initial identification of the number of contributory modes is correct. Although AMI begins like the SDOF methods used historically, in which the contribution of modes other than the one in focus is neglected, the iterative procedure makes it an MDOF algorithm that accounts for coupling between modes.

The procedure will be described briefly here. The discussion will focus on a new, global, SIMO implementation. Differences between this and the SISO implementation of AMI will be highlighted. The data analyzed in AMI consists of the frequency response of all measurement degrees of freedom (DOF) to a harmonic force at the Pth measurement DOF. (By reciprocity this is equivalent to the response of the Pth DOF to a force applied to each measurement DOF sequentially.) It is assumed that the system dynamics can be represented by the familiar second

order matrix differential equation

$$[M]\{\ddot{q}\} + [C]\{\dot{q}\} + [K]\{q\} = \{F\} \tag{1}$$

where $\{q\}$, $[M]$, $[C]$, and $[K]$ are the generalized coordinate vector, and symmetric mass, damping and stiffness matrices respectively each of dimensions $N \times N$. The force vector $\{F\}$ is zero everywhere except the Pth generalized coordinate (or drive point) for a SIMO experiment. When eq. (1) is put into state space form by stacking $\{q\}$ above $\{\dot{q}\}$, the following symmetric generalized eigenvalue problem results

$$[[R] - \lambda[S]]\{\psi\} = \{0\}$$

where $\{\psi\}$ is an arbitrarily scaled mode vector and $[R]$ and $[S]$ are defined as follows.

$$[R] = \begin{bmatrix} [0] & -[K] \\ -[K] & -[C] \end{bmatrix}, \quad [S] = \begin{bmatrix} -[K] & [0] \\ [0] & [M] \end{bmatrix}$$

It can be shown that underdamped modes result in a pair of complex conjugate eigenvalues λ_r whose respective mode vectors $\{\psi_r\}$ are also complex conjugates [18]. The mass normalized mode matrix can then be expressed as

$$[\Psi] = \begin{bmatrix} \{\psi_1\} & \{\psi_2\} & \cdots \end{bmatrix} = \begin{bmatrix} [\phi] & [\phi^*] \\ [\lambda][\phi] & [\lambda^*][\phi^*] \end{bmatrix}$$

where $[\lambda]$ is a diagonal matrix of eigenvalues having positive imaginary parts and $[\phi]$ is the displacement portion of the mode matrix. The frequency response function $\{H_P(\omega)\}$ is the ratio of the complex response amplitude of each generalized displacement to the drive force amplitude. It is related to the state space modal properties by

$$\{H_P(\omega)\} = \sum_{r=1}^{N} \frac{\{A_{P,r}\}}{i\omega - \lambda_r} + \frac{\{A^*_{P,r}\}}{i\omega - \lambda^*_r} \tag{2}$$

$$\{A_{P,r}\} = \lambda_r \{\phi_r\} \phi_{Pr}$$

where λ_r and $\{\phi_r\}$ are the complex eigenvalue and complex normalized eigenvector of the rth mode of vibration. The notation ϕ_{Pr} signifies the Pth element of the rth mode vector, or the Prth element of the displacement portion of the modal matrix, and $\{A_{P,r}\}$ is the Pth column of the residue matrix for mode r. The eigenvalue is related to the natural frequency and damping ratio by: $\lambda_r = -\zeta_r\omega_r \pm \omega_r\left(1-\zeta_r^2\right)^{1/2}$ where ω_r and ζ_r are the rth natural frequency and damping ratio.

AMI proceeds in two stages: Subtraction and Isolation. These stages will be described for the global SIMO implementation, though the overall procedure is similar to the SISO implementation described in previous papers.

3.1 Subtraction Stage

AMI begins with the subtraction stage, in which modes are subtracted from the experimental data one at a time. The algorithm starts by considering the dominant mode, located as the highest peak of the composite FRF, where the composite FRF is defined as the sum of the magnitude of the FRFs for all response points,

$$H_c(\omega) = \sum_{j=1}^{N_o} |H_{jP}(\omega)| \tag{3}$$

with N_o being the number FRFs. The SISO implementation of AMI operated successively on a single FRF, and thus did not consider a composite FRF.

Data in the vicinity of the peak in the composite FRF is sent to an SDOF fitting algorithm (described subsequently) that returns the eigenvalue and mode vector that best fit the dominant mode in all FRFs. The number of data points around the peak that are fit is a compromise between averaging out noise (more points) and reducing the contribution of other modes (fewer points). For the problems presented in this paper the half power points were used, defined as all points near the peak such that

$$H_c(\omega) > \alpha * \max(H_c(\omega)) \tag{4}$$

where $\alpha = 0.707$.

An FRF model for the fit mode is then constructed using eq. (2), and the fit mode is subtracted from the FRF data. This brings the mode having the next highest peak into dominance. This mode is also identified and subtracted from the data. The process continues until the composite FRF shows no coherent peaks suggestive of the presence of additional modes. Presently, this is determined by visual inspection of the data.

3.2 Mode Isolation Stage

Once all of the modes of the system have been approximated, the estimate for each mode is refined through an iterative procedure. At this stage the algorithm proceeds through the modes in the sequence of their dominance in the composite FRF. The contributions of all modes except for the one in focus are subtracted from the FRF data. This leaves only the experimentally measured contribution of the mode in focus, as well as noise and any errors that may exist in the fit of the other modes. The mode in focus is then re-fit using the SDOF fitting algorithm. At this point, the data essentially contains only one mode, so an SDOF fit yields an improved estimate of the current mode's parameters. Also, because the contribution of all other modes has presumably been removed from the data, the fitting algorithm can now consider more data around the peak, further minimizing the effects of noise. Care should be taken however. Because of the limited resolution of sensors and data acquisition equipment, data very far from the peak may not be reliable. For the problems presented subsequently, the criteria in eq. (4) was applied with $\alpha = 0.5$, (fitting the data above the quarter-power points rather than the half power points.) In [13], Ginsberg et al found that this was optimum for a single FRF contaminated with random, white noise.

The model is then updated with the modal parameters fitting the mode in focus, and the algorithm proceeds to the next mode. A cycle through all identified modes constitutes one iteration. Typically only a few iterations are required. Computations cease when convergence criteria for the eigenvalues and residues have been met.

3.3 SIMO SDOF Fitting Algorithm

The extension of AMI from SISO to SIMO is achieved by expanding the data set and vectorizing the algorithm. It invokes a (non-iterative) linear-least-squares fit. Considering only the rth mode in eq.(2), and placing the two terms associated with this mode on a common denominator yields

$$\{H_P(\omega)\} = 2\frac{i\omega \operatorname{Re}(\{A_P\}) - \operatorname{Re}(\{A_P\}\lambda^*)}{|\lambda|^2 - \omega^2 - 2i\omega \operatorname{Re}(\lambda)} \tag{5}$$

Note that the subscript r has been dropped because only one mode is considered. Clearing the denominator in eq. (5) and breaking the result into real and imaginary parts then leads to

$$\operatorname{Re}[\{H_P(\omega)\}]\left(|\lambda|^2 - \omega^2\right) + 2\omega \operatorname{Im}[\{H_P(\omega)\}] \operatorname{Re}(\lambda) = -2\operatorname{Re}(\{A_P\}\lambda^*) \tag{6}$$

$$\operatorname{Im}[\{H_P(\omega)\}]\left(|\lambda|^2 - \omega^2\right) - 2\omega \operatorname{Re}[\{H_P(\omega)\}] \operatorname{Re}(\lambda) = 2\omega \operatorname{Re}(\{A_P\}) \tag{7}$$

The resulting system of equation is linear in $|\lambda|^2$, $\operatorname{Re}(\lambda)$, and in the vector variables: $\operatorname{Re}(\{A_P\})$, and $\operatorname{Re}(\{A_P\}\lambda^*)$. In matrix form this can be expressed as:

$$\begin{bmatrix} \operatorname{Re}\{H_P(\omega)\} & 2\omega \operatorname{Im}\{H_P(\omega)\} & 2[I] & [0] \\ \operatorname{Im}\{H_P(\omega)\} & -2\omega \operatorname{Re}\{H_P(\omega)\} & [0] & -2\omega[I] \end{bmatrix} \begin{Bmatrix} |\lambda|^2 \\ \operatorname{Re}(\lambda) \\ \operatorname{Re}\{A_P\} \\ \operatorname{Re}(\{A_P\}\lambda^*) \end{Bmatrix} = \begin{Bmatrix} \omega^2 \operatorname{Re}\{H_P(\omega)\} \\ \omega^2 \operatorname{Im}\{H_P(\omega)\} \end{Bmatrix} \tag{8}$$

where the identity matrices $[I]$ and zero matrices $[0]$ are all of dimensions $N_o \times N_o$. The matrix on the left hand side and the vector on the right hand side of eq. (8) are both known at a number of discrete frequencies. These are evaluated at $L > 1$ discrete frequencies near a resonance and stacked resulting an the overdetermined linear system denoted as follows.

$$[\alpha]_{(2N_oL)\times(2N_o+2)} \{x\}_{(2N_o+2)\times 1} = \{\beta\}_{(2N_oL)\times 1} \tag{9}$$

The parameters $\{x\}$ that minimize the squared fit error in eq. (9) are found to be

$$\{x\} = \left([\alpha]^T [\alpha]\right)^{-1} \left([\alpha]^T \{\beta\}\right) \tag{10}$$

The solution to eq. (10) can be made more computationally efficient by expressing the elements of the products $[\alpha]^T [\alpha]$ and $[\alpha]^T \{\beta\}$ in terms of the raw data, rather than actually forming $[\alpha]$ and $\{\beta\}$ and evaluating the products. Furthermore, the product matrices can be computed directly with minimal operations because a number of elements of $[\alpha]$ and $\{\beta\}$ cancel or are multiplied by zero when the products are evaluated. The overall fitting process is very efficient and requires little computation time. Because a large number of frequencies are typically used, (i.e. $L >> 1$), this results in a substantial reduction in the size of the fitting matrix.

The global SIMO algorithm described above resembles the rational fraction polynomial (RFP) method, restricted to a single degree of freedom. Despite this similarity, the differences in computation time and performance are great. The RFP algorithm needs orthogonal polynomials to improve numerical conditioning. The polynomials must be orthogonal with respect to the data set, and so significant computational effort is involved in finding them. Even then, ill conditioning occurs as the model order, and hence the powers in the polynomials, increase. Because the global SIMO algorithm above is limited to a single degree of freedom, the highest power of ω that occurs is ω^2, so ill conditioning is not an issue. Also, because only SDOF fits are used in the fitting process, memory does not limit the maximum number of modes that can be fit as with many MDOF methods (SSI or ERA for example). This may eliminate the need to analyze data in blocks or to analyze band-pass filtered subsets of data, as is often done with popular MDOF algorithms.

The performance of AMI-SIMO relative to the rational fraction polynomial and stochastic subspace algorithms will be evaluated in later sections through the use of an analytical test problem that allows for a definite assessment of accuracy.

4 Test Problem: Cantilevered Frame

4.1 Frame System Description

No single test problem can capture every difficulty that could occur in a real experiment. The present problem has been used [14], [15], [10] to assess the performance of previous implementations of AMI . The intent is to capture the effect of varying noise levels, weakly excited modes, and close modes. The problem was described in detail in [10], where the SISO version of AMI was used with the identical data set. The problem consists of two orthogonal cantilevered beams, welded at their free ends, seen in Figure 1. Each beam has a solid circular cross section with 100 mm radius, modulus of elasticity $E = 70 \times 10^9$ Pa, modulus of rigidity $G = 26.32 \times 10^9$ Pa, and 2700 kg/m^3 density. The span lengths are set at $L_1 = 4$ m, $L_2 = 3.85$ m. Two transverse dampers, $c_1 = c_2 = 155.88$ N-s/m, oriented out-of-plane are placed at $x_1 = 4$ m and $x_2 = 3$ m. In addition, two torsional dampers, $c_3 = c_4 = 77.94$ N-s-m/rad, are placed at $x_1 = x_2 = 1$ m. The dashpots provide non-proportional viscous damping. (In this problem

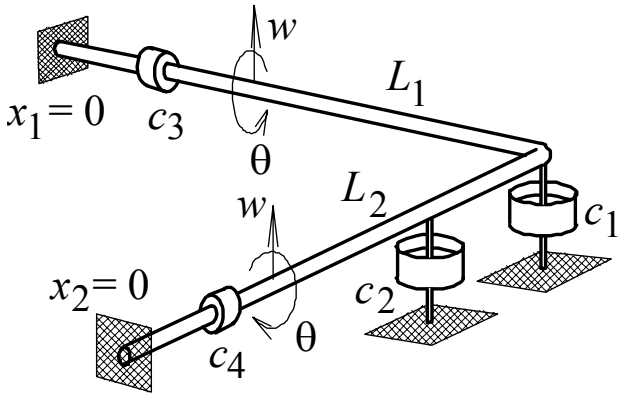

Figure 1: Cantilevered Frame System

damping is light, so a proportional damping model based on diagonalizing the modal damping matrix [18] would give similar results.) The slight deviation from symmetry (due to slightly different beam lengths) results in modes 8 and 9 having highly localized high frequency patterns and close natural frequencies.

The Ritz method is used to model the system. The problem couples bending and torsion, so a Ritz series is used for both bending and torsional deformation of each beam (total of four Ritz series). The Ritz series is used to construct

Mode	**Re{λ}**	**Im{λ}**	$Damp$ $\zeta * 100$
1	-0.656461	68.0047	0.97
2	-0.164031	265.912	0.06
3	-0.482573	386.324	0.12
4	-0.267046	829.451	0.03
5	-0.793483	1033.75	0.08
6	-0.610694	1697.01	0.04
7	-3.1205	1937.89	0.16
8	-18.7961	2479.67	0.76
9	-18.1254	2510.98	0.72
10	-5.34622	2995.66	0.18
11	-5.21094	3380.04	0.15

Table 1: Eigenvalues for First 11 Modes

the system matrices, from which the state-space modal properties of the system are found. For a more detailed description of the system and modeling, see [14], [15]. Also, this problem is presented as an exercise in Ginsberg [18], though with different system parameters. The Ritz analysis results in a set of analytical modal parameters. The eigenvalues for the lowest 11 modes are shown in Table 1.

Truncation of each Ritz series at 11 terms was found to yield convergent results for the lowest 21 modes. These were used to construct the time domain response due to a unit impulsive force in the first beam, one meter from the clamped support. (The unconverged modes were at frequencies well beyond the range of interest.) Using the Ritz series, the displacement and rotation as a function of time at 7 points on the structure due to the impulsive force were obtained. The resulting response vector $\{y(t)\}$ contains both displacements and rotations at locations one meter apart,

$$\{y(t)\} = [w_1\ w_2\ w_3\ w_4\ \theta_1\ \theta_2\ \theta_3\ \theta_4\ w_5\ w_6\ w_7\ \theta_5\ \theta_6\ \theta_7\ \theta_8]^{\mathrm{T}} \tag{11}$$

where the first 8 elements are measured on the first beam and the last 7 elements are measured on the second beam.

The analytical responses were sampled, and then noise contaminated by adding zero-mean, normally distributed white noise scaled to have a standard deviation of 1% of the maximum of each impulse response. The noise contaminated impulse responses were then transformed to frequency response functions (FRFs) via a Fast Fourier Transform (FFT). The sample rate and sample time were chosen to satisfy the Nyquist criterion and minimize leakage in the FFT.

4.1.1 Response Data

The resulting noise-contaminated and clean FRFs for the drive point (the first measurement DOF) are shown in Figures 2 and 3. A zoom view is included, which focuses on the response of the close modes 8 and 9.

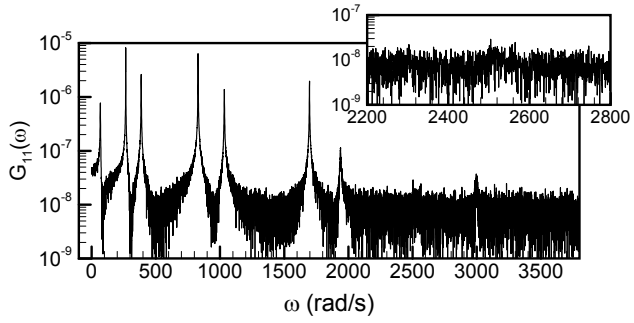

Figure 2: Noisy displacement FRF at $x = 1$ m on beam 1.

Eleven modes are present in the frequency band of interest. The high frequency modes (8-11) are barely visible in

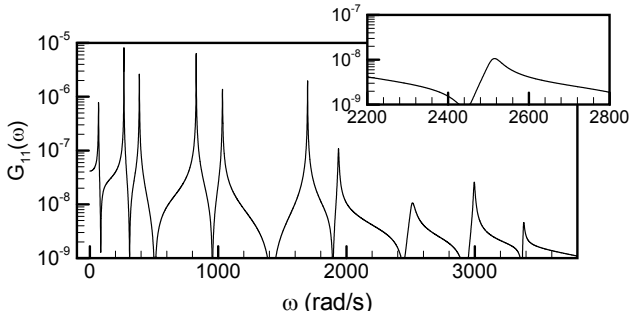

Figure 3: Clean displacement FRF at $x = 1$ m on beam 1.

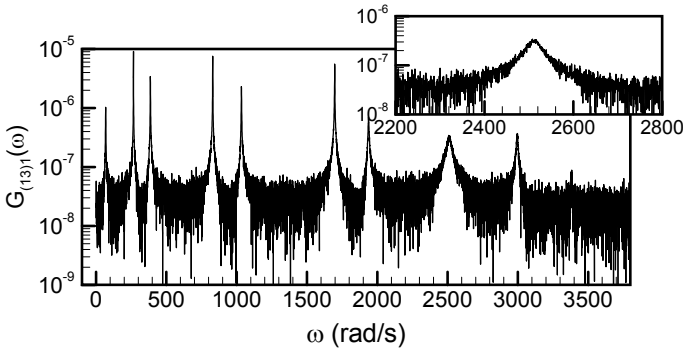

Figure 4: Noisy rotation FRF at $x = 2$ m on beam 2.

the noise-contaminated data. In contrast, the higher frequency modes are fairly well represented in the rotation data, as evidenced in Figure 4. Only a single peak is evident due to modes 8 and 9. These figures are typical of all of the data. There is a large range in effective noise amplitude in the vicinity of the resonance peaks. The signal to noise ratios at the peaks of the FRFs range from 60-40 dB for the dominant, low frequency modes, and from 20 dB to negative for the weakly excited, high frequency modes.

4.2 Analysis with Peak-Picking Method

To aid in assessing the results that follow, the peak-picking and half-power bandwidth methods were used on the composite FRF to find the natural frequencies and damping ratios of the system modes, which yields estimated eigenvalues. Because no peak is evident in the composite FRF in the vicinity of mode 8, it was missed. The average of the absolute value of the errors in the real and imaginary parts of the eigenvalues for the first seven modes were 10% and 0.039% respectively. These were dominated by errors in modes 1 and 4 because of the coarseness of the FRF in the vicinity of these peaks. Without these modes the average errors drop to 2.3% and 0.010%. For modes 9-11 the average errors are, 11% and 0.025%.

4.3 Analysis with SIMO-AMI

The FRFs for frequencies from 0 to 3800 rad/s (8589 data points per FRF) were analyzed with AMI in an interactive mode. After each subtraction step, a user examined the composite FRF and decided whether to continue to look for more modes. Ten modes were identified in the subtraction stage of AMI. Mode 8 is buried in noise in the composite FRF after all other modes were removed, so it was missed completely.

For illustrative purposes, the composite FRF is plotted against the fit composite for the last few subtraction steps. Figure 5 shows the composite residual versus fit for the 8th mode that was found (analytical mode 10). The points used in the fit (the half power points) are accented as well. The residual after removing the 8th mode and the fit on the 9th mode (analytical mode 9) are shown in Figure 6. Figure 7 shows the next subtraction step. Figure 7 also illustrates the severe effect of the noise on the data away from resonance, as only the peak data resembles the reconstructed response.

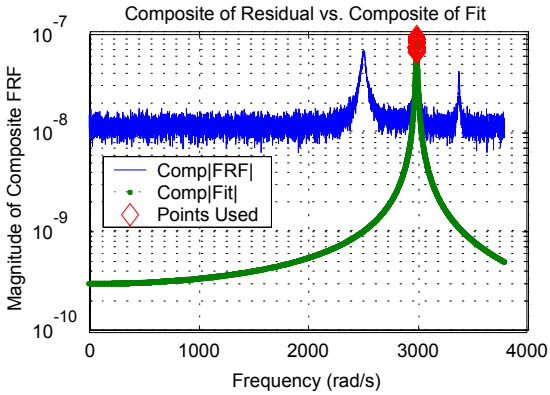

Figure 5: AMI - Composite Residual FRF and single mode fit at the eighth subtraction step, which identifies analytical Mode 10.

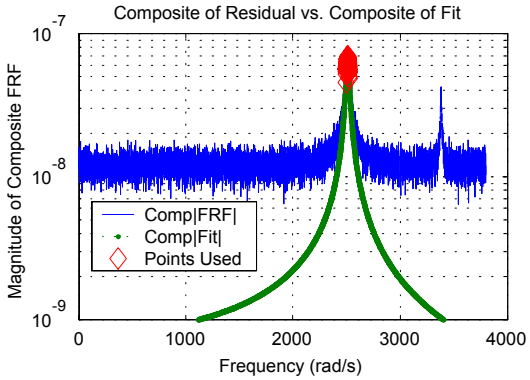

Figure 6: AMI - Composite Residual FRF and single mode fit at the ninth subtraction step, which identifies analytical Mode 9.

In Figure 7 the data seems to have been reduced to noise, except for the peak to which the 11th analytical mode is fit. A very small bump is evident in the data where the 8th mode should be. The presence of mode 8 in the data has adversely affected the estimation of mode 9, causing AMI to overestimate the residue at the response points where mode 8 is active and reducing the accuracy of the 9th eigenvalue. This occurs because AMI is trying to fit a single mode to the response of two modes. If mode 8 were identified during the subtraction stage, these errors could be eliminated in the mode isolation stage, when the contributions of other modes are accounted for. Because mode 8 is not identified, its presence is not accounted for in the mode isolation stage, and the parameters of mode 9 remain in error. Even then, the estimates of the ninth eigenvalue and mode shape are good considering the noise.

Table 2 shows the percent errors obtained in the eigenvalues by both the global SIMO-AMI algorithm and the local, SISO AMI algorithm. In all tables error is defined as: $e_{pct} = (identified - true) * 100/true$. Notice that in all tables the percent errors in the imaginary parts have been multiplied by 1000. The errors for the SISO and SIMO algorithms are comparable, though the global algorithm is more accurate on average, especially for the lower frequency modes. Both algorithms are about 2 orders of magnitude more accurate than the peak picking method for the first seven modes. The non-global, SISO AMI algorithm has the advantage that it identified the highly localized mode 8, albeit with considerable error. A significant advantage of the global algorithm is that user interaction and processing time were greatly reduced. With the local algorithm it was often difficult to tell when to stop looking for modes, and the decision had to be made for each FRF individually. With the global algorithm there was no ambiguity concerning when to stop looking for modes, as illustrated in Figure 7.

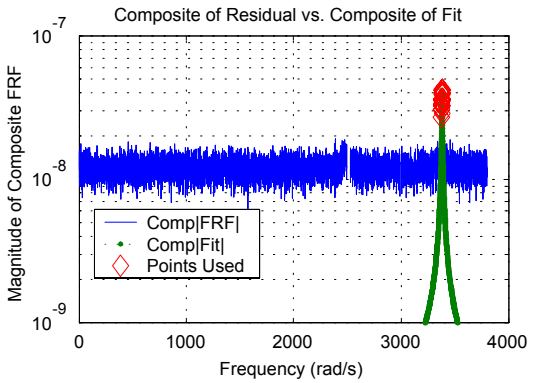

Figure 7: AMI - Composite Residual FRF and single mode fit at the tenth subtraction step, which identifies analytical Mode 11.

SIMO-AMI (Global AMI)		SISO AMI (Non-Global)	
Re	**Im*1000**	**Re**	**Im*1000**
0.01%	0.25%	0.11%	-0.22%
0.01%	-0.01%	-0.06%	-0.10%
-0.07%	0.08%	-0.22%	-2.05%
0.04%	0.01%	0.01%	-0.03%
0.02%	0.16%	0.08%	-0.28%
0.03%	-0.03%	-0.13%	-0.07%
-0.35%	-0.69%	1.72%	-1.30%
missed	missed	-21.71%	-450.32%
8.04%	26.43%	3.82%	7.51%
4.10%	3.81%	5.23%	-6.60%
26.86%	-15.94%	8.15%	-9.75%

Table 2: Percent Errors in Eigenvalues From Global and Non-Global AMI

4.4 Analysis with RFP

A global, SIMO version of the Rational Fraction Polynomial algorithm was also used to fit the data. A multitude of variations on the RFP algorithm exist in the literature. Formenti and Richardson [19] give references to 60 citations of the algorithm in IMAC proceedings. The algorithm used in this paper was programmed in Matlab based on the presentation in Maia et al [20]. This incorporated a number of improvements described by Formenti and Richardson [19], including orthogonal polynomials, global curve fitting, and extra numerator terms. The latter had no noticeable effect on the results for this problem because the modes can be separated into uncoupled groups where out of band modes have very little effect.

Despite the implementation of orthogonal polynomials, the global RFP solution became ill conditioned for a simultaneous fit of more than 9 or 10 modes. Consequently, it was decided to break the frequency range of interest into at least three bands and fit each band individually. The analysis presented here used the following bands: ([0 to 1300], [1300 to 2250], and [2250 to 3800] rad/s) Even then, RFP would just barely converge on the modes of interest before numerical ill-conditioning occurred. Figure 8 shows the stabilization diagrams for each band, concatenated onto a single figure, with solid (red) vertical lines indicating the divisions between bands. The composite FRF is superimposed.

A number of spurious modes are identified at the beginning and end of the analysis bands. These are especially troublesome because they are stable with model order, so they are hard to tell from true system modes. A single mode is identified in the vicinity of close modes 8-9. Eigenvalues for modes 10 and 11 do not stabilize well enough for these to be detected with any confidence. Even the most accurate eigenvalues found on the stabilization diagram were much less accurate than those found by AMI or SSI. The poor performance of the RFP algorithm is probably best

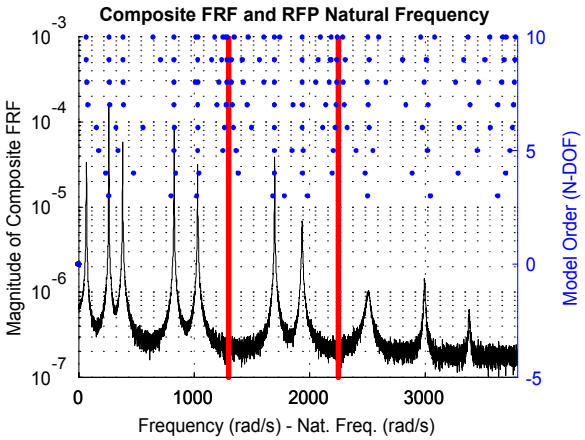

Figure 8: Stabilization diagram from RFP algorithm, processed in bands. Solid red lines indicate the divisions between analysis bands.

explained by the fact that RFP minimizes a weighted error function. The fit error is weighted by the denominator of the FRF (see eq. (2)). The denominator is small near resonance, so the result is a fit where the data away from resonance is weighted more heavily than the data at resonance. RFP performs fairly well when applied over small bands in which a single mode or a number of coupled modes are active. Also, iterative procedures are available for improving RFP's weighting.

4.5 Analysis with SSI

The Stochastic Subspace Identification algorithm [5] was also used to process the noise contaminated analytical data. The specific stochastic algorithm used was included in the software tools supplied with [5] implemented in the function "subid.m." The algorithm was explored extensively in order to optimize the identification.

Subspace identification is a two stage process. A greatly simplified explanation follows. For more detail, see [3] or [5]. The time domain output data is arranged in a large block Hankel matrix. (A Hankel matrix is a matrix where each antidiagonal consists of a repetition of the same element [21].) In the first stage, geometric projection yields the Kalman filter states for a bank of nonsteady Kalman filters acting down the columns of the Hankel matrix. This basically serves to filter the data, where anything not coherent with the response of a linear time invariant system is removed from the data. The effectiveness of this filtering is dependent on the number of block rows i in the data Hankel matrix, and is proven to be unbiased as $i \to \infty$. Computation time scales with i^2. Geometric projections are implemented using QR and Singular Value decompositions. The projections result in the state sequence, that is, the response of the system expressed in terms of a set of state variables. The states are sorted based upon the magnitude of their corresponding singular values. The user then may set the model order by truncating the state sequence to include only the dominant states (or modes). One of a number of least squares solutions then extracts the system matrices from the truncated state sequence. An eigenvalue solver can then be used to find the natural frequencies, damping ratios and mode shapes from the system matrices.

For modal analysis problems of 20 response points or more, computer memory can be a limiting factor in obtaining good results. Because this problem used relatively few responses, good results could be obtained using the limited memory available. Only the first 8192 points of the time domain impulse response were processed, though no improvement was seen by using more data. (This is comparable to the amount of data processed by AMI, though AMI processed frequency data.) The algorithm documentation suggested a formula for determining the number of block rows to use: $i = 2 * (maxorder) / (\#outputs)$ where $maxorder$ is the maximum model order to be estimated and $\#outputs$ is the number of outputs (15 in this case). For 11 modes and 15 outputs $i = 1.5$. Trial and error discovered that the algorithm performed poorly unless many more block rows ($i \geq 32$) were used. Analyses were performed on a machine with 384 Megabytes of RAM. Available memory limited the number of block rows to just over 64.

With $i = 32$ the performance of SSI is remarkable. The stabilization diagram shown in Figure 9 shows the natural

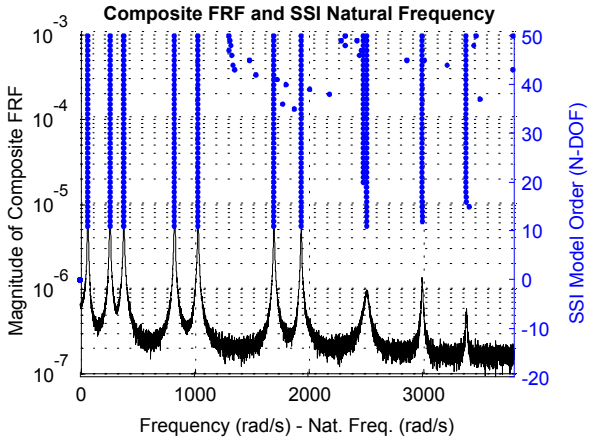

Figure 9: Stabilization Diagram for SSI algorithm with 32 Block Rows

SIMO-AMI (Global AMI)		SSI ($i = 32$) $N = 21$ modes	
Re	**Im*1000**	**Re**	**Im*1000**
0.01%	0.25%	4.1%	16.3%
0.01%	-0.01%	0.9%	0.8%
-0.07%	0.08%	1.3%	2.0%
0.04%	0.01%	-2.6%	-1.2%
0.02%	0.16%	0.4%	0.3%
0.03%	-0.03%	-1.2%	0.5%
-0.35%	-0.69%	-2.4%	-0.4%
missed	missed	-11.4%	89.0%
8.04%	26.43%	-0.3%	45.1%
4.10%	3.81%	-1.5%	4.7%
26.86%	-15.94%	4.5%	6.2%

Table 3: Errors in Eigenvalues, SIMO-AMI and SSI

frequencies identified for model orders ranging from 10 to 50. The composite FRF is overlaid.

Only a small number of computational modes are identified in the frequency range of interest, though the true modes are easily discernible. All modes are identified, including the highly localized, weakly excited mode 8. The high quality of the results is not surprising. The data is contaminated only by the addition of white noise, which excludes more troublesome errors, such as leakage, anti-alias filtering [4], nonlinearity, etc... SSI is based upon a model that includes zero-mean, random white noise, and it is proven to be convergent as the dimensions of the data Hankel matrix approach infinity. Note also that all modes are not identified for model orders below 20, though only 11 modes are present in the band of interest. Recall that 21 modes were used in constructing the analytical impulse response. The time domain data processed by SSI was not filtered to limit the effect of modes outside of the band of interest. In a real problem, the true model order is infinite, and anti-aliasing filters or digital filters may be used to reduce the effect of modes outside the frequency range of interest. In such a case, SSI would need to identify all poles of the digital filter before absolute convergence could be obtained as in Figure 9, so this quality of results is not likely to be possible for real problems.

Table 3 shows the error in the real and imaginary parts of the eigenvalues found by both SIMO-AMI and SSI. (Errors in the natural frequency and damping ratio are comparable to the errors in the imaginary and real parts respectively.) Both algorithms are quite accurate for the first 7 modes, where the FRFs are clean, with the errors for SIMO-AMI being 1-2 orders of magnitude smaller than SSI. SSI identifies mode 8, and more accurately identifies the real parts of the 9th and 10th eigenvalues, and the 11th eigenvalue. When compared to the peak picking method, SSI's eigenvalues are order of magnitude more accurate on average, though the errors for many of the specific modes are comparable between the two methods.

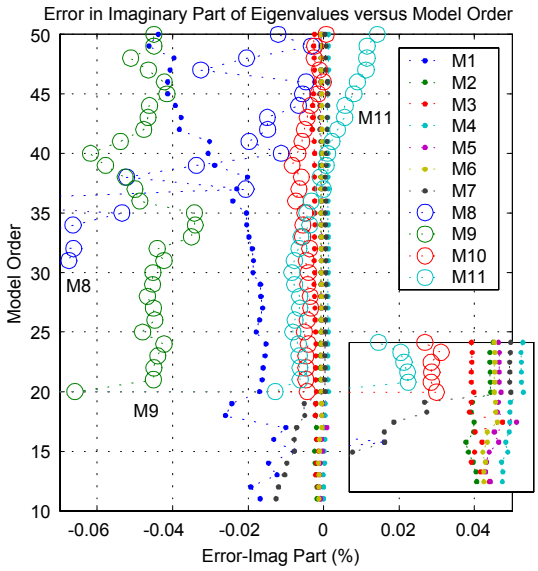

Figure 10: Errors (%) in the Imaginary parts of the eigenvalues identified by SSI with 32 block rows.

The errors in the real parts of SSI's eigenvalues (damping ratio) for the first seven modes are quite good, but for some applications they may be significant. If the true eigenvalues were not known, it is unlikely that these errors would have been suspected. Furthermore, increasing the size of the data matrix would significantly increase the computation time for the SSI algorithm. Hence, when reasonable results are obtained, a user is unlikely to increase the matrix size further.

In order to see if the stabilization diagram gives any indication that less than optimum results have been obtained, the errors in the imaginary parts of the eigenvalues are plotted versus model order in Figure 10. If the bias is ignored, each branch is equivalent to what one would see when zooming in on a particular branch of the stabilization diagram. The least accurate eigenvalues seem to vary most with frequency, though for model orders between 20 and 30 all eigenvalues but the 8th do not change much. The zoom view on the behavior of modes 1-7 shows that they converge abruptly at a model order of 21 and then don't appear to vary appreciably. In a real problem with infinite degrees of freedom this would occur gradually and convergence would only be reached if all modes present in the data and data filters were identified. Even then, bias errors such as slight nonlinearities in the structure or sensors might adversely affect the results. A plot for the real parts shows similar trends. There is no evidence of the relatively large bias errors in modes 1-7 on the stabilization diagram. The drift in the first, eighth and eleventh eigenvalues might suggest the need for more block rows, though one would expect these modes to be less accurate because their signal to noise ratios are much smaller. Also, the drift is not large in an absolute sense.

Using a larger number of block rows in the data Hankel matrix improves the results for the SSI algorithm. The stabilization diagram for $i = 64$ is shown in Figure 11. A comparable number of computational modes appeared in the SSI results for $i = 64$ as for $i = 32$. In Figure 11, all modes for which $\zeta > 0.05$ were removed. For this problem, this single pole rejection criteria eliminates all computational modes from the frequency band of interest. Verboven et al [7] [22] and Goethals et al [6] have examined the problem of detecting spurious poles.

Use of 64 block rows modestly reduced the error in the eigenvalues identified by SSI. These are shown in Table 4. The number of block rows could not be increased further because of memory limitations.

The behavior of the eigenvalues with model order for $i = 64$ is also considered for comparison with the previous case. Figure 12 shows the error in the imaginary parts of the eigenvalues as a function of model order. Once again, mode 1, and the high frequency modes 8, 9, 10, and 11 are the least accurate. (Mode 8 is off the chart.) The eigenvalues are now more stable with model order, relative to their bias errors. If the true eigenvalues were not known, only a very careful inspection of the stabilization diagrams in Figures 9 and 11 would have revealed the trends that are

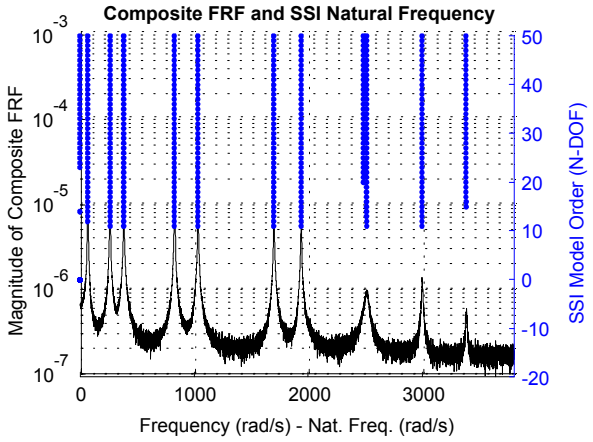

Figure 11: Stabilization Diagram for SSI algorithm with 64 Block Rows. (Modes with $\zeta > 0.05$ removed.)

SIMO-AMI (Global AMI)		SSI ($i = 64$) $N = 21$ modes	
Re	**Im*1000**	**Re**	**Im*1000**
0.01%	0.25%	-0.24%	5.79%
0.01%	-0.01%	-3.27%	-0.71%
-0.07%	0.08%	0.23%	0.002%
0.04%	0.01%	-1.51%	-0.36%
0.02%	0.16%	-1.07%	-0.55%
0.03%	-0.03%	1.96%	0.35%
-0.35%	-0.69%	1.59%	0.34%
missed	missed	13.16%	111.48%
8.04%	26.43%	-0.14%	-3.93%
4.10%	3.81%	0.92%	7.03%
26.86%	-15.94%	10.22%	16.45%

Table 4: Errors in Eigenvalues, AMI-SIMO and SSI

evident in Figures 10 and 12.

Figures 10 and 12 indicate that scatter in the eigenvalues with model order might reveal when less than ideal results have been obtained, though this does not give a good indication of the absolute error in the eigenvalues. The usual practice of creating a single stabilization diagram for a given number of block rows in the data Hankel matrix leads to a false sense of security when it comes to the absolute accuracy of the estimates. A better practice might be to vary both model order and the number of block rows, though this would increase the computation time greatly.

The average of the absolute values of the errors for eigenvalues 1-7 and 9-11 for each method are presented in Table 5. Doubling the number of block rows used by the SSI algorithm has cut the errors in the imaginary parts approximately in half. For modes 1-7, SSI gives estimates of both real and imaginary parts that are an order of magnitude more accurate than the peak-picking method. AMI gives eigenvalue estimates that are two orders of magnitude more accurate than the peak-picking method. For modes 9-11 the trends are different. All methods show errors of about the same order of magnitude as the peak picking method.

5 Computational Effort

For the test problem above AMI was the fastest algorithm. All computations were performed on a machine with an AMD-K7 processor and 384 Megabytes of RAM, using Windows 2000 and Matlab 6.1. AMI required less than one minute of computation time in mode isolation and refinement to converge on accurate modal parameters. Little

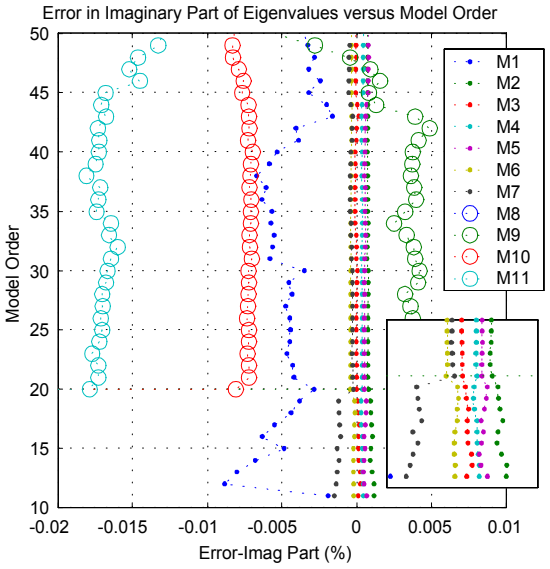

Figure 12: Errors (%) in the Imaginary parts of the eigenvalues identified by SSI with 64 block rows.

Average % Error in Real Parts				
Modes	**Peak Pick**	**SIMO AMI**	**SSI (i=32)**	**SSI (i=64)**
1-7	9.7 %	0.1 %	1.8 %	1.4 %
9-11	11.0 %	13.0 %	2.1 %	3.8 %

Average % Error in Imaginary Parts * 1000				
Modes	**Peak Pick**	**SIMO AMI**	**SSI (i=32)**	**SSI (i=64)**
1-7	38.5 %	0.2 %	3.1 %	1.2 %
9-11	25.3 %	15.4 %	18.6 %	9.1 %

Table 5: Average Percent Errors in Eigenvalues

computation was required during the subtraction stage, though the current version required user interaction to decide when to stop looking for modes.

The RFP algorithm used here was not optimized for Matlab as well as either AMI or SSI. The Matlab implementation of RFP took approximately ten minutes to process the data, though an optimized implementation may have been faster.

SSI was the most computationally intense algorithm. The QR and singular value decompositions took up the bulk of the computation time. For $i = 32$, 2.6 minutes of computation time were required to perform the decompositions and find the system eigenvalues for model orders ranging from 10 to 50. For $i = 64$, 12.6 minutes of computation time were required. While the differences between AMI and SSI in computation time are significant, memory requirements were found to be the limiting factor in analyses with the SSI algorithm. Because only a limited number of response points was used, good results were obtainable with the SSI algorithm within the constraint of physical memory. AMI used orders of magnitude less memory than SSI or the rational fraction polynomial method, so it could have reliably fit many more response points N_o and frequencies L than used in this problem.

6 Conclusion

A simple, computationally efficient, global single–input-multi-output SDOF fitting algorithm has been presented and implemented as a part of the Algorithm of Mode Isolation. (AMI) The resulting SIMO-AMI algorithm was found

to give more accurate results than a SISO-AMI algorithm for the test structure's dominant modes. For the weakly excited modes, the SISO algorithm sometimes gave more accurate results. The SIMO algorithm missed one weakly excited mode because it's response fell below the noise in the composite FRF. This reveals that, although modes are global properties of a structure, when measurement noise is significant, localized modes might be processed most accurately if the data that is fit pertains only to the degrees of freedom in which these modes are active. One benefit of the global algorithm is a great reduction in user interaction when compared to the SISO AMI algorithm.

The SIMO-AMI algorithm was found to give much more accurate results than the Rational Fraction Polynomial (RFP) algorithm for noise contaminated analytical data. This comparison is significant because the RFP algorithm is similar to AMI in mathematical form, though RFP attempts to identify all modes simultaneously.

The SSI algorithm identified the weakly excited mode 8, which was missed by SIMO-AMI, though the computation time for the SSI algorithm was longer. The results demonstrated the importance of considering both model order and the number of block Hankel rows used in the SSI fitting process. A stabilization diagram for a single number of block rows may give a false sense of security as to the accuracy of the modal parameters identified.

When compared to the peak picking method, SSI and AMI respectively estimated the eigenvalues of modes 1-7 with one and two orders or magnitude more accuracy. For modes 9-11 the improvements over the peak-picking method were not as drastic.

The comparison of AMI and SSI should not necessarily be one of competition, as the best features of each algorithm could be incorporated into a single algorithm if desired. For example, to improve it's performance in the presence of noise, AMI could be used to process the FFT of the state sequences found in the first stage of stochastic subspace identification. Conversely, the accuracy of the eigenvalues found by SSI could be improved by using SSI's eigenvalues as a starting point for the mode isolation and refinement stage of AMI. Perhaps the most notable contribution of AMI is that it provides a different way of looking at the problem of modal identification, in which the importance of each mode to the experimental fit is clearly visible.

ACKNOWLEDGEMENT OF SUPPORT

This material is based on work supported under a National Science Foundation Graduate Research Fellowship.

References

[1] R. J. Allemang, *Vibrations Course Notes*. Cincinnati: http://www.sdrl.uc.edu/, 1999.

[2] R. J. Allemang and D. L. Brown, "A unified matrix polynomial approach to modal identification," *Journal of Sound and Vibration*, vol. 211, no. 3, pp. 301–322, 1998.

[3] K. D. Cock, B. Peeters, A. Vecchio, B. D. Moor, and H. V. D. Auweraer, "Subspace system identification for mechanical engineering," *Proceedings of ISMA2002 - International Conference on Noise and Vibration Engineering*, vol. III, (Leuven, Belgium), pp. 1333–1352, 2002.

[4] S. W. Doebling, K. F. Alvin, and L. D. Peterson, "Limitations of state-space system identification algorithms for structures with high modal density," *12th International Modal Analysis Conference (IMAC-12)*, (Honolulu, Hawaii), pp. 633–640, 1994.

[5] P. Van Overschee and B. De Moor, *Subspace Identification for Linear Systems: Theory-Implementation-Applications*. Boston: Kluwer Academic Publishers, 1996.

[6] I. Goethals and B. D. Moor, "Model reduction and energy analysis as a tool to detect spurious modes," *Proceedings of ISMA2002 - International Conference on Noise and Vibration Engineering*, vol. III, (Leuven, Belgium), pp. 1307–1314, 2002.

[7] P. Verboven, E. Parloo, P. Guillame, and M. V. Overmeire, "Autonomous modal parameter estimation based on a statistical frequency domain maximum likelihood approach," *19th International Modal Analysis Conference (IMAC-19)*, (Kissimmee, Florida), pp. 1511–1517, 2001.

[8] H. V. D. Auweraer, W. Leurs, P. Mas, and L. Hermans, "Modal parameter estimation from inconsistent data sets," *18th International Modal Analysis Conference (IMAC-18)*, (San Antonio, Texas), pp. 763–771, 2000.

[9] M. V. Drexel and J. H. Ginsberg, "Mode isolation: A new algorithm for modal parameter identification," *Journal of the Acoustical Society of America (JASA)*, vol. 110, no. 3, pp. 1371–1378, 2001.

[10] M. S. Allen and J. H. Ginsberg, "A linear least-squares version of the algorithm of mode isolation," Submitted, 2004.

[11] Y.-D. Joh and C.-W. Lee, "Excitation methods and modal parameter identification in complex modal testing of rotating machinery," *International Journal of Analytical and Experimental Modal Analysis*, vol. 8, no. 3, pp. 179–203, 1993.

[12] W. F. Pratt, M. S. Allen, and S. D. Sommerfeldt, "Testing and characterization of wavy composites," in *46th International SAMPE Symposium and Exhibition 2001 a Materials and Processes Odyssey*, vol. 46 I, (Long Beach, CA), pp. 216–229, 2001.

[13] J. H. Ginsberg, M. S. Allen, A. Ferri, and C. Moloney, "A general linear least squares sdof algorithm for identifying eigenvalues and residues," *21st International Modal Analysis Conference (IMAC-21)*, (Orlando, Florida), 2003.

[14] M. V. Drexel and J. H. Ginsberg, "Modal parameter identification using state space mode isolation," *19th International Modal Analysis Conference (IMAC-19)*, (Orlando, FL), 2001.

[15] M. V. Drexel, J. H. Ginsberg, and B. R. Zaki, "State space implementation of the algorithm of mode isolation," *Journal of Vibration and Acoustics*, vol. 125, pp. 205-213, 2003.

[16] J. H. Ginsberg, B. R. Zaki, and M. V. Drexel, "Application of the mode isolation algorithm to the identification of a complex structure," *20th International Modal Analysis Conference (IMAC-20)*, (Los Angeles, CA), pp. 794–801, 2002.

[17] J. H. Ginsberg and M. S. Allen, "Recent improvements of the algorithm of mode isolation," *Proceedings of IMECE'03, ASME International Mechanical Engineering Congress and Exposition, NCA*, (Washington, DC), 2003.

[18] J. H. Ginsberg, *Mechanical and Structural Vibrations*. New York: John Wiley and Sons, 2001.

[19] D. Formenti and M. Richardson, "Parameter estimation from frequency response measurements using rational fraction polynomials (twenty years of progress)," *20th International Modal Analysis Conference (IMAC-20)*, (Los Angeles, CA), pp. 373–382, 2002.

[20] S. Maia, J. M. M. Silva, J. He, N. A. Lieven, R. M. Lin, G. W. Skingle, W. M. To, and A. P. V. Urgueira, *Theoretical and Experimental Modal Analysis*. Taunto, Somerset, England: Research Studies Press Ltd., 1997.

[21] B. Peeters and G. D. Roeck, "Reference based stochastic subspace identification for output-only modal analysis," *Mechanical Systems and Signal Processing*, vol. 13, no. 6, pp. 855–878, 1999.

[22] P. Verboven, P. Guillame, E. Parloo, and M. V. Overmeire, "Autonomous structural health monitoring–part 1:modal parameter estimation and tracking," *Mechanical Systems and Signal Processing*, vol. 16, no. 4, pp. 637–657, 2002.